Ultrasmall Ga-ICG nanoparticles based gallium ion/photodynamic synergistic therapy to eradicate biofilms and against drug-resistant bacterial liver abscess

Tingting Xie [a,b], Yuchen Qi [b], Yangyang Li [b], Feilu Zhang [c], Wanlin Li [b], Danni Zhong [b], Zhe Tang [d], Min Zhou [a,b,*]

[a] Eye Center, The Second Affiliated Hospital, Zhejiang University School of Medicine, Hangzhou, 310009, China
[b] Institute of Translational Medicine, Zhejiang University, Hangzhou, 310009, China
[c] Department of Surgery, The Second Affiliated Hospital, Zhejiang University School of Medicine, Hangzhou, 310009, China
[d] Department of Surgery, The Fourth Affiliated Hospital, Zhejiang University School of Medicine, Yiwu, 322000, China

ARTICLE INFO

ABSTRACT

Pyogenic liver abscess and keratitis are aggressive bacterial infections and the treatment has failed to eradicate bacteria in infectious sites completely owing to the currently severe drug resistance to existing antibiotics. Here, we report a simple and efficient one-step development of ultrasmall non-antibiotic nanoparticles (ICG-Ga NPs) containing clinically approved gallium (III) (Ga^{3+}) and liver targeting indocyanine green (ICG) molecules to eradicate multi-drug resistant (MDR) bacteria thought the synergetic effect of photodynamic therapy and iron metabolism blocking. The ICG-Ga NPs induced photodynamic effect could destroy the bacterial membrane, further boost the endocytosis of Ga^{3+}, then replace iron in bacteria cells to disrupt bacterial iron metabolism, and demonstrate the synergetic bacterial killing and biofilm disrupting effects. The ICG-Ga NPs show an excellent therapeutic effect against extended spectrum β-lactamases *Escherichia coli* (ESBL *E. coli*) and significantly improve treatment outcomes in infected liver abscess and keratitis. Meanwhile, the ultrasmall size of ICG-Ga NPs could be cleared rapid via renal clearance route, guaranteeing the biocompatibility. The protective effect and good biocompatibility of ICG-Ga NPs will facilitate clinical treatment of bacteria infected diseases and enable the development of next-generation non-antibiotic antibacterial agents.

1. Introduction

Pyogenic liver abscess (PLA) is a suppurative infection of the liver parenchyma, which may cause serious complications [1–3]. With the increasing number of patients with diabetes and biliary diseases, the prevalence of PLA presents a general uptrend [4]. Clinically available antibiotics are the main methods for treating liver infections [5]. However, multiple drug-resistant (MDR) bacteria and highly virulent pathogenic bacteria have been gradually emerging due to the heavy use of antibiotics [6,7] Some faced problems, such as multiple drug resistance and systemic toxicity, lead to the therapeutic failure of existing antibiotics [8,9] Despite massive efforts to find new antibiotics, the development of new drugs is still far behind the evolution of antibiotic resistance. Therefore, it is urgent to develop high-efficiency non-antibiotic based strategies against bacterial liver abscess.

Many non-antibiotic antibacterial agents, such as antibacterial peptides [10,11], polymers [12], and inorganic nanoparticles (NPs) [13–17], have shown great potential as antibacterial materials over the past few decades. Among them, the rapid development of inorganic non-antibacterial agents, including silver [18,19], copper [20,21], and gold NPs [22,23], have been widely utilized in the field of wound dressings and surgical devices, which exhibited effective antibacterial therapeutics performance. However, currently reported inorganic anti-bacterial agents are mainly applied in the field of wound infection [24–26]. There are still some biosafe concerns about whether these metal-based antibacterial agents (particularly Ag NPs) can be used to give full scope to antibacterial ability in internal organ infection [27–29]. Till now, there are few reports about the treatment for bacterial

induced liver abscess by using any non-antibiotic agent, including nanoparticles.

Recently, gallium compounds have been proved the antibacterial activity against a number of pathogenic bacteria, and also have a good effect on a variety of animal infection models [30–33]. Importantly, information about the interaction between gallium and bacterial iron metabolism has been obtained, which demonstrated gallium could disrupt iron-associated metabolism processes of bacteria [34–36]. Thus, gallium compounds exhibited effective antibacterial activity against many pathogens, especially for MDR bacteria. However, the *in vivo* targeted therapy is not good for the reported gallium compounds owing to the low delivery efficiency to the infected tissues. Also, few works about the gallium-based nanoagents that can target to the infected tissue for curing bacterial infections so far have reported. Indocyanine green (ICG), an FDA approved near-infrared (NIR) fluorescent dye, has been clinically applied in the diagnosis of liver function owing to its active liver targeting property [37]. [[,38] [][][]] Moreover, ICG is a photosensitizing agent that has been frequently used for photodynamic therapy (PDT) based on its ability to produce reactive oxygen species (ROS) under NIR laser irradiation [39]. [[,40] [][][]] Amusingly, ICG-based nanoscale coordination particles have demonstrated prominent performance in the control of bacterial infection, which has led to little antibiotic resistance. The membrane components of bacteria could be damaged by the generated ROS so that the antibacterial gallium component can enter and play a synergistic therapeutic effect. Therefore, we explore the gallium-based inorganic-organic hybrid antimicrobial nanoparticles, with a simple composition and structure, based on Ga^{3+} and ICG molecule by an aqueous synthesis (Scheme 1).

2. Materials and methods

2.1. Materials

Chemicals, including indocyanine green (ICG) and gallium chloride ($GaCl_3$), were purchased from Sigma-Aldrich. Phosphate buffer saline (PBS), physiological saline (NaCl) solutions and Dulbecco's Modified Eagle Medium (DMEM) were acquired from Sinopharm Chemical Reagent Co. Ltd. 3-(4,5-Dimethyl-2-thiazolyl)-2,5-diphenyl-2H-tetrazolium bromide (MTT) assays kit, LIVE/DEAD Backlight Bacterial Viability kits, and DCFH-DA Kits were purchased from Thermo Fisher Scientific (China). Lysogeny broth (LB) broth medium was purchased from Biomerieux. Hepl liver cells, Human Embryonic Kidney 293 (HEK 293) cells, Human Umbilical Vein Endothelial (HUVEC) cells, and Human Immortalized Keratinocytes (HaCaT) cells were obtained from the American type culture collection. β-lactamase-producing *Escherichia coli* (ESBL *E. coli*) was obtained from the American type culture collection
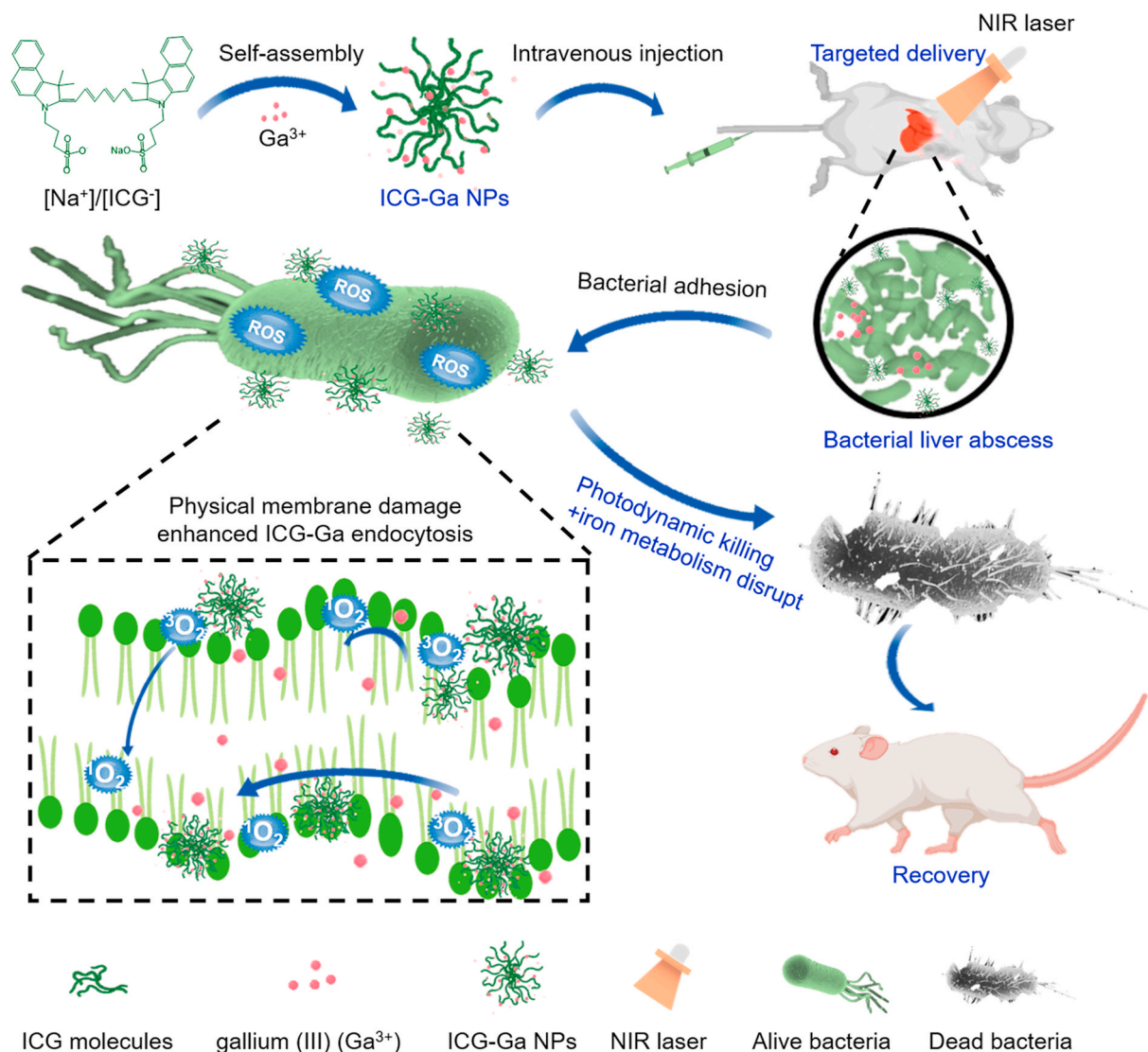
Scheme 1. Schematic illustration synthesis of ICG-Ga NPs and served as a non-antibiotic antimicrobial agent to treat drug-resistant bacterial infected liver abscess.

(ATCC 25922).

2.2. Synthesis of ICG-Ga nanoparticles (NPs)

Briefly, 10 mg ICG powder was dissolved in 100 mL ultra-pure water to form the uniform ICG solution (100 mg/L). Subsequently, 1.4 mL gallium chloride (GaCl$_3$) solution (5 mg/mL) was slowly added to the above ICG solution. Under the condition of avoiding light, the mixture was further stirred for 3 h at room temperature. Finally, ICG-Ga nanoparticles were obtained by centrifugation-filtration through 30 kDa MWCO Amicon filters (Sigma-Aldrich) and stored at 4 °C for further characterization.

2.3. Cell culture

All cells were cultured in DMEM medium containing 10% fetal bovine serum and 1% anti-bis (penicillin-streptomycin) and placed in a 37 °C incubator with 95% O$_2$ and 5% CO$_2$. The cells were collected by centrifugation (1000 rpm 3 min) and subcultured with 0.25% trypsin until the confluence reached about 80%.

2.4. Cytotoxicity evaluation

The cytotoxicity of ICG-Ga to Hepl cells, HEK 293 cells, HUVEC cells, and HaCaT cells was tested by a standard MTT assay. Cells were seeded in 96-well plates (100 μL/well, 8.0×10^4 cells/mL) and cultured for 12 h in a 37 °C incubator. Then the medium was removed and cells were treated with ICG-Ga NPs dispersed in fresh medium with different concentrations (0, 4.16, 8.32, 16.6, 33.28, 66.56, 133.12, and 266.24 μg/mL) for an additional 24 h. Furthermore, MTT solution (20 μL, 5 mg/mL) was added to replace the medium and they were incubated for another 4 h. The medium was discarded again and 150 μL dimethylsulfoxide (DMSO) was added to each well to dissolve the formazan, with shaking for at least 15 min. The corresponding spectra absorption at 570 nm wavelength was recorded with a microplate reader (SpectraMax, MD M5, the USA).

2.5. In vitro preliminary evaluation of antibacterial efficiency of ICG-Ga NPs

EBSL *E. coli* was selected to assess the synergistic antibacterial effects of ICG-Ga NPs. 20 μL EBSL *E. coli* in the phase of logarithmic growth were seeded into tubes in a biochemical incubator after mixing 8 mL of LB broth medium. Subsequently, 100 μL bacterial suspension was transferred into 96-well plates after treating with different concentrations (0, 3.125, 6.25, 12.5, and 25 μg/mL) of ICG-Ga NPs for 24 h. The optical absorbance at 600 nm (OD$_{600}$) wavelength was measured by a multimode microplate reader (SpectraMax, MD M5, the USA) to indicate the bacteria concentration. Each concentration group was arranged parallel wells without bacteria (OD$_{600}$ = OD$_{600 \text{ experiment}}$ - OD$_{600 \text{ background}}$) to deduct the background absorption of materials.

2.6. In vitro evaluation of photodynamic antibacterial efficiency of ICG-Ga NPs

EBSL *E. coli* were irradiated by an 808 nm laser with series of optical intensity (0, 0.1, 0.25, 0.5, 0.75, and 1 W/cm^2) for 10 min after inoculating with 25 μg/mL ICG-Ga NPs for 2 h and cultured for another 24 h in a 37 °C biochemical incubator.100 μL bacterial suspension form the treated EBSL *E. coli* was transferred into 96-well plates to measure the OD$_{600}$, indicating the bacteria concentration for further estimating survival rates, by a multimode microplate reader (SpectraMax, MD M5, the USA). Each concentration group was arranged parallel wells without bacteria (OD$_{600}$ = OD$_{600 \text{ experiment}}$ - OD$_{600 \text{ background}}$) to deduct the background absorption of materials.

2.7. In vitro evaluation of synergistic antibacterial efficiency of ICG-Ga NPs

EBSL *E. coli* was irradiated by an 808 nm laser at the 1 W/cm^2 optical intensity for 10 min after inoculating with 25 μg/mL ICG-Ga NPs or ICG for 2 h and cultured for another 24 h at a 37 °C shaking incubator. OD$_{600}$ was measured by a microplate reader (SpectraMax, MD M5, the USA). Each concentration group was arranged parallel wells without bacteria to deduct the background absorption of materials (OD$_{600}$ = OD$_{600 \text{ experiment}}$ - OD$_{600 \text{ background}}$). Meanwhile, 10 μL bacterial suspensions from the above EBSL *E. coli* were serially diluted 10^6-fold to LB broth medium according to a doubling dilution method. The number of diluted bacteria solutions was determined by the standard plate counting method. The clone plates were taken photos and counted. Each group had three replicates.

2.8. LIVE/DEAD staining was used to examine bacterial viability

1.5 mL EBSL *E. coli* with 10^7 CFU received an 808 nm laser radiation at the1 W/cm^2 optical intensity for 10 min after inoculating with 25 μg/mL ICG-Ga NPs or ICG for 2 h the EBSL *E. coli* then collected and rinsed with NaCl solutions twice times after culturing for another 2 h at a 37 °C shaking incubator. SYTO9 and propidium iodide (50 μL 30 μM) dyes were used to stain for 15 min. Samples were observed under an inverted fluorescence microscope (Leica DMI 4000B, Germany).

2.9. Detection of reactive oxygen species (ROS) in bacteria

2′,7′-Dichlorodihydrofluorescein (DCFH-DA, Sigma-Aldrich) was used to detect the oxidative oxygen species generated by various treatments in bacteria cells. To be specific, EBSL *E. coli* was irradiated by an 808 nm laser for 10 min at the 1 W/cm^2 optic intensity after inoculating with 25 μg/mL ICG-Ga NPs or ICG for 2 h at a 37 °C shaking incubator. Then treated ESBL *E. coli* were stained immediately for 30 min by adding DCFH-DA dye to bacterial suspension. The bacteria suspensions were centrifuged (8000 rpm, 5 min) and redispersed in PBS. Respectively, fluorescence microscope (Leica DMI 4000B, Germany) and flow cytometry (Cytoflex Beckman America) were utilized to observe and quantify the green fluorescence of ROS.

2.10. Bacterial scanning electron microscopy (SEM) and transmission electron microscope (TEM)

2 mL ESBL *E. coli* with 10^6/CFU were inoculated into tubes in a biochemical incubator after mixing 2 mL LB broth medium and received an irradiation form an 808 nm laser at the 1 W/cm^2 optical intensity for 10 min after exposing to 2 mL ICG-Ga NPs or ICG at the concentration of 25 μg/mL for 2 h. Bacterial suspensions were collected by centrifugation (8000 rpm, 5 min) and fixed in 2.5% glutaraldehyde solutions for 12 h, and immobilized again with 1% osmium tetroxide solution for another 1–2 h. The bacteria were rinsed with PBS three times after each fixation. Subsequently, a gradient of concentration ethanol (30%, 50%, 70%, 80%, 90%, 95% and 100%) was used to dehydrate for 15 min. Critical point dry was carried out in a critical point dryer (Hitachi HCP-2-type, Japan). Finally, samples were observed by scanning electron microscope (Hitachi SU-8010, Japan). For the TEM, the above-dehydrated sample further was embedded with Spurr embedding agent and sliced by a cutter (Leica EM UC7, Germany). The slices of samples were stained by citric acid solution and uranyl acetate for 10 min and observed by transmission electron microscope (Hitachi H-7650, Japan).

2.11. Biofilm inhibition assays

Biofilms were formed on coverslips horizontally suspended in 6-well plates. Each coverslip was inoculated with ~2×10^6 CFU/mL of ESBL *E. coli* in LB broth medium at a 37 °C biochemical incubator. The culture

medium was changed every day until the biofilm was formed. The supernatant in each well was removed and 3 mL of LB medium containing ICG-Ga NPs or ICG at the concentration of 25 μg/mL was added into each well of 6-well plates until ESBL *E. coli* biofilms formed. The wells were irradiated by an 808 nm laser at a power density of 1.0 W/cm^2 for 10 min after incubation with ICG-Ga NPs or ICG for 2 h. The treated biofilms were stained by SYTO9 solutions for 15 min. For 3D confocal laser scanning microscopy(CLSM)image observation, 3D images of the stained biofilms were obtained by a laser confocal scanning microscope (Leica TCS SP8, Germany), and data were analyzed by using the LAS X software.

2.12. In vivo evaluation of antibacterial efficiency of ICG-Ga NPs

All animal experiments were approved by the Institutional Animal Care and Use Committee of Zhejiang University School of Medicine. The therapeutic efficacy of ICG-Ga NPs was assessed on a well-established liver abscess model. Briefly, 8 weeks-old female Balb/c mice were purchased from Shanghai SLAC animal experiments Limited. The mice were injected with 50 μL ESBL *E. coli* (1.0×10^7 CFU/mL) in liver parenchyma to form abscess, and randomly divided into five groups for the different treatments (n = 5, each group). Respectively. the mice were intravenously administrated with 200 μL ICG and ICG-Ga NPs (100 μg/mL) after infection with bacteria, and irradiated with an 808 nm laser at a power density of 1.0 W/cm^2 for 10 min. As a control, saline was injected into the infected mice. After all kinds of treatments for day 1 and day 3, the livers were harvested and broken by TissuePrep disintegrator to thoroughly disperse bacteria with PBS. The number of bacteria was determined by the standard plate counting method. Meanwhile, the liver tissues from each group were harvested and fixed with 4% formalin solution for hematoxylin & eosin (H&E) staining, immune-histochemical (IL-6 and IL-1b) staining and gram staining. The staining results were observed by using an Olympus IX71 microscope and photographs of those infected liver were taken. The ESBL *E.coli*-infected models mice were injected with 200 μL of 100 μg/mL ICG-Ga NPs and photographed by IVIS Lumina LT Series (Perkin Elmer) at different time points (0, 0.5, 0.5, 1, 2, 4, 8, and 12 h). Major issues of the mice sacrificed after being observed, including the heart, liver, spleen, lung, and kidney, were collected and photographed as well. The data of each photograph was analyzed using Living Image 4.5 software (Perkin Elmer). All experimental procedures involving animals were performed in accordance with the Guidelines for the ethics committee of the Experimental Animal Center of Zhejiang University Institutional.
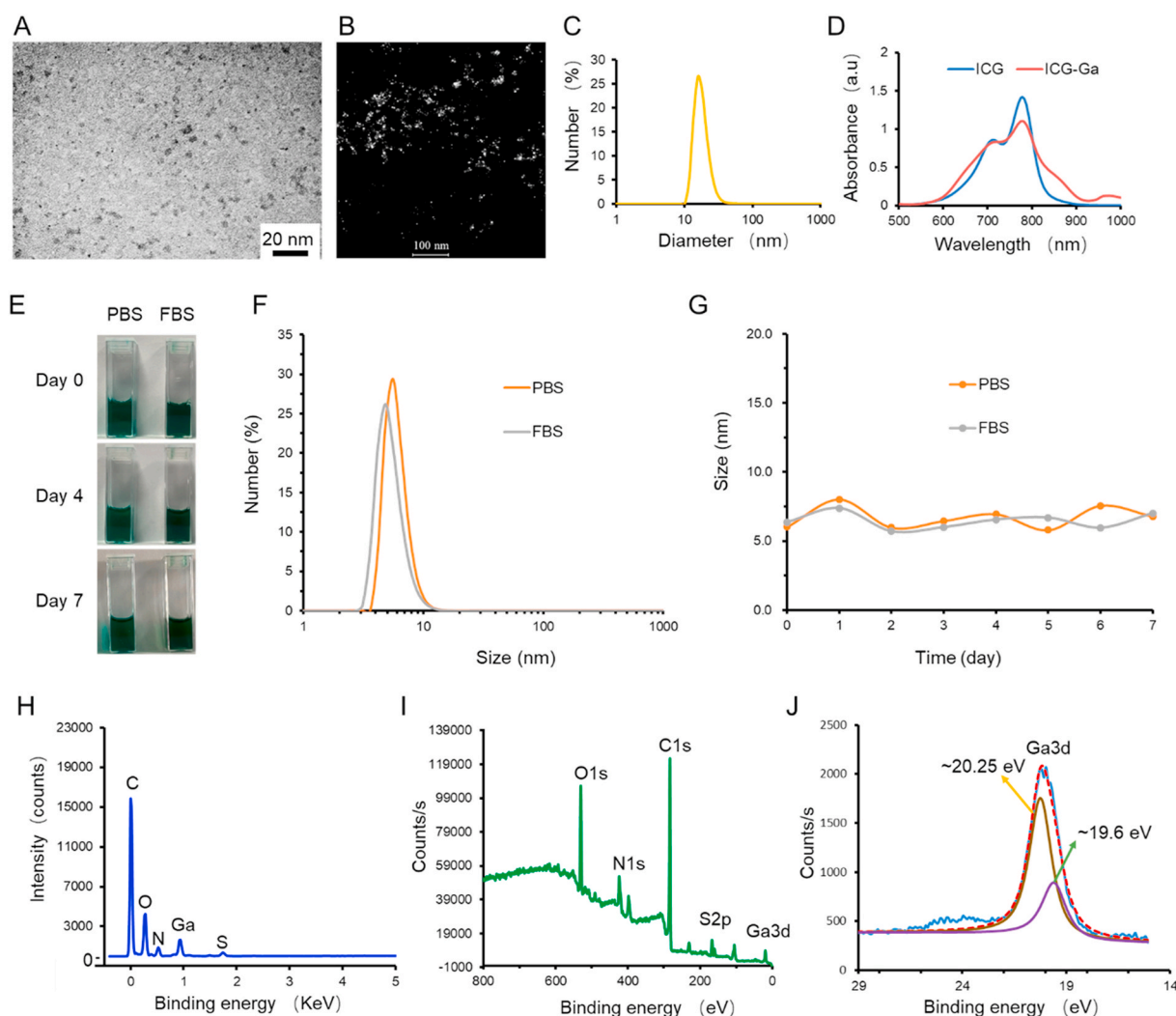
Fig. 1. Characterization of the ICG-Ga NPs. (A) The TEM image of as-synthesized ICG-Ga NPs. (B) Dark field transmission electron microscopy image of the ICG-Ga NPs. (C) DLS distribution of ICG-Ga NPs suspended in aqueous solution. (D) UV–vis absorption spectra of ICG-Ga NPs and ICG solution. Stability of ICG-Ga NPs in PBS and FBS, (E) images of different days, (F) Size distribution and (G) size changes in a week. (H) Energy dispersive X-ray spectroscopy of ICG-Ga NPs. (I, J) XPS spectrum of ICG-Ga NPs and spectra of Ga3d orbits of ICG-Ga NPs for the binding energies together with the fitting curves.

2.13. In vivo preliminary toxicity assessment of ICG-Ga NPs

Bodyweight of the mice was also recorded at the time of administration with 200 μL of 100 μg/mL ICG-Ga NPs. The mice were sacrificed on day 14 and the blood was collected for blood routine, alanine aminotransferase (ALT), aspartate transaminase (AST), blood urea nitrogen (BUN) and creatinine (CREA) examinations. Major issues, including the heart, liver, spleen, lung, and kidney, were harvested for H&E staining. The sections were obtained with an Olympus IX71 microscope.

3. Results and discussion

3.1. Synthesis and characterization

ICG-Ga NPs were prepared *via* one step, metal-coordination assisted self-assembly procedures (Scheme 1). Transmission electron microscopy (TEM) showed shapes of the synthesized ICG-Ga NPs having a homogeneous size distribution and the average size of ICG-Ga NPs was ~5 nm (Fig. 1A and B). However, the size distribution measured by dynamic light scattering (DLS) was ~15 nm (Fig. 1C), which may due to a certain degree of aggregation in aqueous solution. As expected, owing to the high NIR absorbance of ICG molecules, ICG-Ga NPs exhibited an overlapping absorbed peak with pure ICG around 760 nm (Fig. 1D). ICG-Ga NPs can stay stable in PBS and FBS for a week (Fig. 1E–G). Further, energy dispersive spectrometry (EDS) analysis demonstrated the ICG-Ga NPs involve C, O, N, S, and Ga elements (Fig. 1H). In addition, X-ray photoelectron spectroscopy (XPS) measurements were carried out to further confirm the composition of elements, which shows the XPS spectrum of ICG-Ga NPs and the details for the characteristic peaks of O1s, N1s, C1s, S2p, and Ga3d that are well consistent with the composition of ICG-Ga NPs (Fig. 1I). Especially, the Ga3d peak can be deconvoluted into two components [41]. It can be observed that two peaks located at 20.3 and 19.6 eV (Fig. 1J), respectively, which can be attributed to the Ga^{3+} and Ga^{3+} species. Finally, thermogravimetric (TG) tests were carried out to further confirm the ICG molecules have successfully coordinated with Ga ion (Fig. S1).

Four kinds of normal human cells, including human embryonic kidney 293 (HEK 293) cells, Hepl liver cells, human umbilical vein endothelial (HUVEC) cells, and human immortalized keratinocytes (HaCaT) cells were used to investigate the cytotoxicity of ICG-Ga NPs compared with Ag nanoparticles (Ag NPs) (Fig. S2). The relative cell viability of the ICG-Ga NPs group retained over 80% with the increased NPs' (with respect to Ga) concentration from 0 to ~266 μg/mL. However, when examined the concentration of Ag NPs range from 0 to ~266 μg/mL, the cell viability showed obvious cytotoxicity when the Ag NPs concentration reached 33.28 μg/mL. Evenly, ~99% of experimental cells can be killed when the Ag NPs concentration came to ~266 μg/mL. The above results reflected an excellent cytocompatibility of the ICG-Ga NPs.

3.2. In vitro antibacterial activity and destruction of biofilms

The *in vitro* antibacterial efficacy of ICG-Ga NPs against ESBL *E. coli* showed a correlation with the concentration of Ga element, increasing with Ga content range from 0 to 25 μg/mL. Of note, bacterial viability was reduced by about 65% at the gallium concentration of 25 μg/mL (Fig. 2A) because of blocking iron metabolism (Fig. S3). The antibacterial effect of ICG-Ga NPs combined with NIR laser irradiation was evaluated at the Ga concentration of 25 μg/mL. The combination of ICG-Ga NPs and laser irradiation showed bactericidal effects toward ESBL *E. coli* in a laser intensity-dependent manner. The bacterial survival rate was progressively inhibited with the gradually enhanced laser power intensity from 0 to 1 W/cm^2. The relationship of ROS level with time and power is shown in Fig. S4. ~90% of the bacteria were killed when the laser intensity was set at 0.75 W/cm^2. Over 99.5% of the bacteria were

killed when the laser power density reached to 1 W/cm^2 (Fig. 2B). In addition, the temperature variation of bacterial suspension changes slightly under the applied laser power intensity (Fig. S5). The maximum temperature of bacterial suspension is no more than 41 °C even under the condition of 1 W/cm^2 laser irradiation, which indicates that the outstanding antibacterial performance may not be caused by photothermal effect but mainly be attributed to the combination of gallium ion and ICG molecules. Meanwhile, the above results revealed that the power intensity of laser irradiation has significant influences on bactericidal activity.

Subsequently, the irradiation power intensity and concentration of ICG-Ga NPs were respectively fixed at 1 W/cm^2 and 25 μg/mL to investigate the combined antibacterial activity. As shown in Fig. 2C and 60% of bacterial were killed in the ICG-Ga NPs group. Irradiation could promote the release of Ga ion (Fig. S6). However, the enhanced antibacterial ability was observed when ICG-Ga NPs combined an 808-nm laser irradiation, with more than 95% of the bacteria killed in this group. While ICG molecules showed no antimicrobial activity without laser irradiation, and only 30% of the bacteria could be killed in the sole photodynamic group (ICG + Laser). Similarly, the colony formation assay and corresponding bacterial counts of ESBL *E. coli* treated with different methods also demonstrated that there was no significant difference in the number of bacteria between the ICG group and the control group, indicating the alone ICG molecules had no antibacterial effect. The number of bacteria in the ICG + laser group decreased slightly, but it was still significantly (p < 0.05) higher than that in the ICG-Ga NPs group and ICG-Ga + Laser group. ICG-Ga + Laser group possesses the most effective bacteria killing efficiency compared with all other groups, which was reflected by the minimal number of bacterial (Fig. 2D and E). These data demonstrated that the combination ICG-Ga NPs with laser can dramatically inhibit the bacteria activity compared with single antimicrobial treatment. Additionally, the antimicrobial activity of ICG or ICG-Ga NPs with laser irradiation may be attributed to the toxic ROS. Thus, DCFH-DA was utilized to investigate the generation of ROS after different treatments on ESBL *E. coli*. As exhibited in Fig. 2F,G and Fig. S7, the bacteria treated with ICG or ICG-Ga NPs plus laser irradiation present prominent fluorescence signal, demonstrating the speedy performance of ROS generation under laser irradiation. Furthermore, live/dead staining assay was performed to evaluate the bacterial survival rates via detecting the fluorescence. As shown in Fig. 2H and Fig. S8&S9, live/dead staining images of ESBL *E. coli* in control and ICG groups displayed almost no red fluorescence signal, indicating the bacteria were alive. In contrast, some red fluorescence emerged in the ICG + Laser and the ICG-Ga NPs groups, and more red fluorescence signals were observed in the ICG-Ga + Laser group. Those results suggested an excellent antibacterial property of ICG-Ga NPs under the 808 nm irradiation, which was consistent with colony formation assay (Fig. 2D and E). We also compared the antibacterial ability of ICG-Ga NPs with traditional antibiotics. Although both of themed show good performance on normal *E. coli*, penicillin could hardly kill ESBL *E. coli* (Fig. 2I and J). ICG-Ga NPs can also be used in more infections caused by drug-resistant bacteria (Fig. S10).

To further study the antibacterial mechanisms, the morphological variations of ESBL *E. coli* after the different treatments were observed by scanning electron microscopy (SEM), ESBL *E. coli* in the control and the sole ICG groups were in normal clubbed shape and intact smooth surface. However, the original morphology was distorted and displayed a wrinkled bacterial cell wall with clear lesions and holes when the bacteria were irradiated by the 808 nm laser after treating with ICG or ICG-Ga NPs (Fig. 3A). Notably, the relevant mapping analysis of SEM showed that the enhancive Ga^{3+} aggregated on the destroyed bacterial membrane (Fig. 3B), which may boost the endocytosis of Ga^{3+}. Further, the internal morphologies of bacteria were observed by transmission electron microscopy (TEM). The ESBL *E. coli* became irregularly shaped, and partial outer membranes were damaged after treating with ICG plus laser irradiation or ICG-Ga NPs (Fig. 3C). Particularly, the most internal
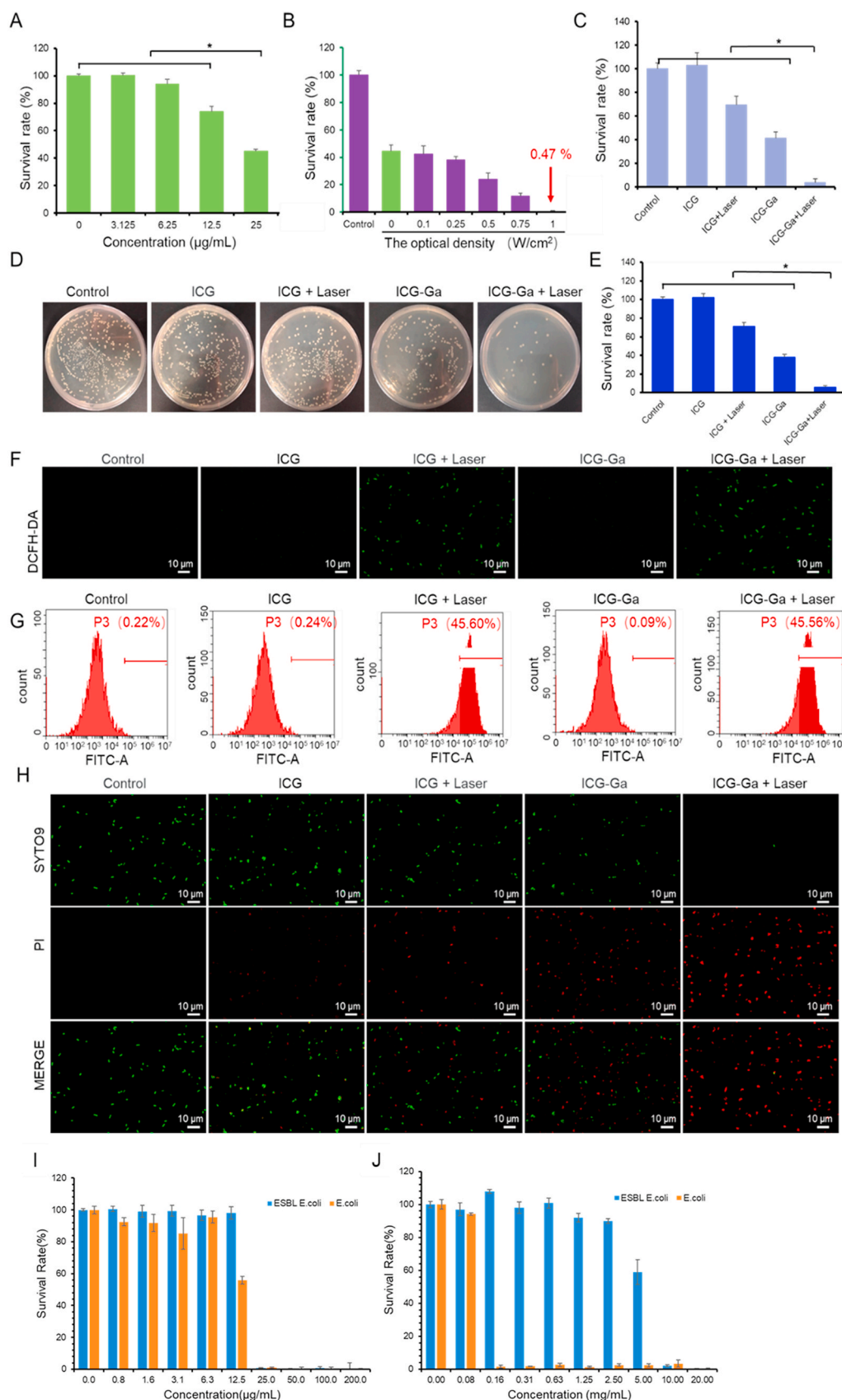
Fig. 2. *In vitro* antibacterial viability of ICG-Ga NPs against ESBL *E. coli*. (A) Survival rates of ESBL *E. coli* after incubation with ICG-Ga NPs at different concentrations (0, 3.125, 6.25, 12.5, and 25 μg/mL) at 37 °C in LB medium for 24 h. (B) Survival rates of ESBL *E. coli* under an 808 nm laser irradiation at the different power intensity (0, 0.1, 0.25, 0.5, 0.75, and 1 W/cm²) after incubation with ICG-Ga NPs of 25 μg/mL at 37 °C in LB medium for 24 h. (C) Survival rates of ESBL *E. coli* irradiated by an 808 nm laser irradiation at the power density of 1.0 W/cm² for 10 min after incubation with 25 μg/mL ICG-Ga NPs or ICG. (D) optic photographs of bacterial colonies formed by the treated ESBL *E. coli* in all groups and (E) the corresponding CFU counts. (F) Fluorescent images of ESBL E. coli, stained by DCFH-DA, upon an 808 nm laser irradiation (1 W/cm², 10 min) after incubation with 25 μg/mL ICG-Ga NPs or ICG. (G) Flow cytometry analysis of ESBL E. coli quantifies the generation of ROS by staining with DCFH-DA. (H) The fluorescence images of the treated ESBL *E. coli*, stained by SYTO9 and propidium iodide (PI) dyes. (*p < 0.05) Comparison of In vitro antibacterial ability on ESBL E. coli and E. coli between (I) ICG-Ga NPs and (J) Penicillin.
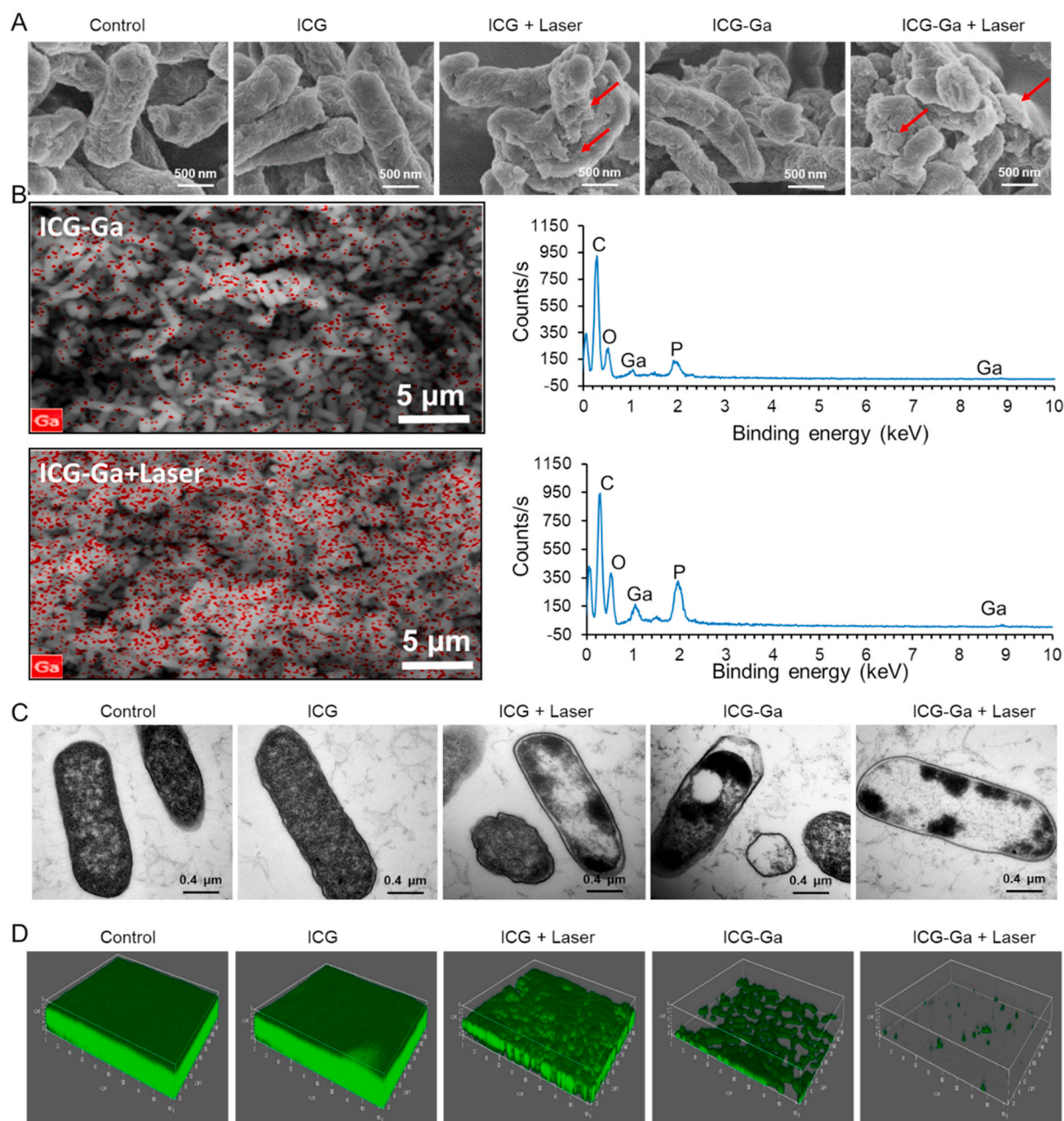
Fig. 3. *In vitro* bactericidal effect and inhibiting biofilm formation of ICG-Ga NPs against ESBL *E. coli*. (A) The SEM images of ESBL *E. coli* after different treatment and (B) the respective mapping analysis. (C) TEM images of the treated ESBL *E. coli*. (D) 3D confocal laser scanning microscopy images (size: 630 μm × 630 μm) of ESBL *E. coli* biofilms after different treatments. Biofilms were stained by SYTO9. The live bacteria can be observed with green fluorescence.

contents of bacteria disappear and membranes were destroyed partially after treating with ICG-Ga NPs plus laser irradiation, indicating the loss of structural integrity of cell walls [42]. Bacterial biofilms are a major cause of drug resistance. Thus, the eliminating effect of ICG-Ga NPs on biofilms was further assessed. As shown in Fig. 3D, the green fluorescence means the live bacteria among the biofilms. The addition of gallium could effectively suppress the growth of ESBL *E. coli* biofilms compared with the control and the ICG groups. The biofilm is almost completely eliminated and can be barely formed in the ICG-Ga + Laser pattern. Therefore, ICG-Ga with laser treatment revealed the synergistically antibacterial effect of Ga-based therapy and photodynamic therapy, which leads to the severe destructions on bacterial biofilms.

3.3. In vivo biodistribution

Given the exciting results *in vitro*, a series of examinations using the ESBL *E. coli*-infected liver abscess of mouse model was carried out to investigate the *in vivo* conjunctively antibacterial effect of ICG-Ga NPs. Initially, to observe and analyse the biodistribution and metabolic behaviour of ICG-Ga NPs *in vivo*, the characteristics of NIR absorption and fluorescence emission of ICG molecules were utilized to monitor the biodistribution. Subsequently, mice infected by ESBL *E. coli* were administered with 200 μL of IGG-Ga NPs (100 μg/mL) and imaged via an optical imaging system at different time points (Fig. 4A). Within the initial 0.25 h after administration, strong fluorescence signals were detected in the abdominal area of mice and reached the maximum value soon afterward. Therefore, the signal weakened gradually at the time point of 0.5–8 h and ultimately disappeared at 12 h. The variations of
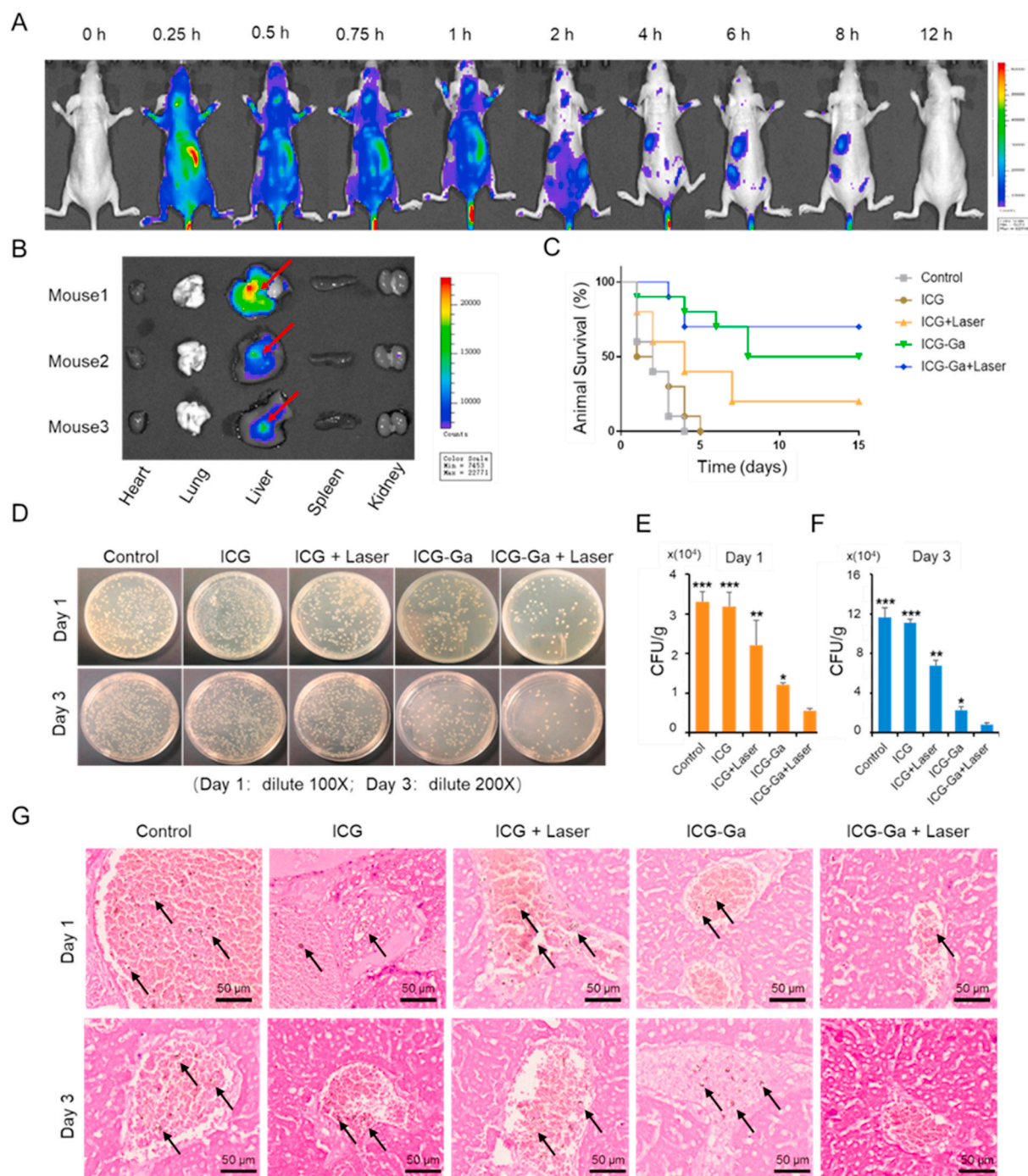
Fig. 4. *In vivo* therapeutic effects of ICG-Ga NPs. (A) Biodistribution of ICG-Ga NPs post-injection in mouse models of liver abscess. Fluorescence images at different times (0, 0.25, 0.5, 0.75, 1, 2, 4, 6, 8, and 12 h) in ESBL *E. coli* infected mouse models after intravenous injection with ICG-Ga NPs. (B) *Ex vivo* Fluorescence images of the major organs (heart, lung, liver, spleen, and kidney) in ESBL *E. coli* infected mouse after injection with ICG-Ga NPs for 2 h (n = 3), red arrow: liver abscess. The ICG-Ga NPs could accumulate at the infection area. (C) Survival rates curve of the infected mice after treatments (n = 10). (D) The optical images of bacterial colonies formed on LB agar plates on day 1 and day 3 after various treatments. (E, F) The corresponding CFU counts of ESBL *E. coli* of the bacterial colonies, (n = 3). (G) The Grams staining of livers section at day 1 and day 3 after various treatments (Bacteria were pointed out with black arrows). (*$p < 0.05$, **$p < 0.01$, ***$p < 0.001$).

fluorescence intensity may be caused by the biodistribution behaviour of ICG-Ga NPs in mice. At the time point of 0.25, 2, and 6 h, the mice were sacrificed to harvest heart, liver, spleen, lung, and kidney. The fluorescence signals of those major organs were detected by the same imaging system (Fig. 4B and Fig. S11). The *in vivo* fluorescence images demonstrated that ICG-Ga NPs rapidly accumulated in liver tissue and reached the peak value within 0.25 h. Subsequently, it was quickly removed away from the body of mice, leading to the decreasing accumulation,

which was attributed to the clearance characteristics by hepatic and renal metabolism. As expected, the higher liver fluorescence signal was observed consistent with the whole-body fluorescent images. Therefore, those results demonstrated that ICG-Ga NPs can be located at the liver sites to treat the bacterial infection.

3.4. In vivo antibacterial activity

It was proved that the laser of 808 nm could penetrate the abdomen of mice and function on the affected area in Fig. S12. The survival rates of the infected mice irradiated by the 808 nm laser at a 1 W/cm^2 power intensity for 10 min after administering with 200 μL of PBS, ICG (100 μg/mL), or ICG-Ga NPs (100 μg/mL) respectively was carefully investigated, as demonstrated in Fig. 4C. Mice in the control and the ICG groups died successively from day 1 to day 3 or 4, respectively.

Especially, most of mice died in day 1 and day 2, demonstrating that the sole ICG was ineffective in treating acute hepatic abscess caused by ESBL *E. coli.* In the ICG + Laser and ICG-Ga NPs groups survival rates were respective 20% and 50%, indicating the gradually enhanced treatment effect. Encouragingly, the eventual survival rate in the ICG-Ga + Laser group was 70%, which was significantly higher than all other groups. The above results directly reflect the excellent ESBL *E. coli* killing performance of ICG-Ga NPs combined with PDT treatment. The liver tissues were later made into homogenates for colony counting to quantify the
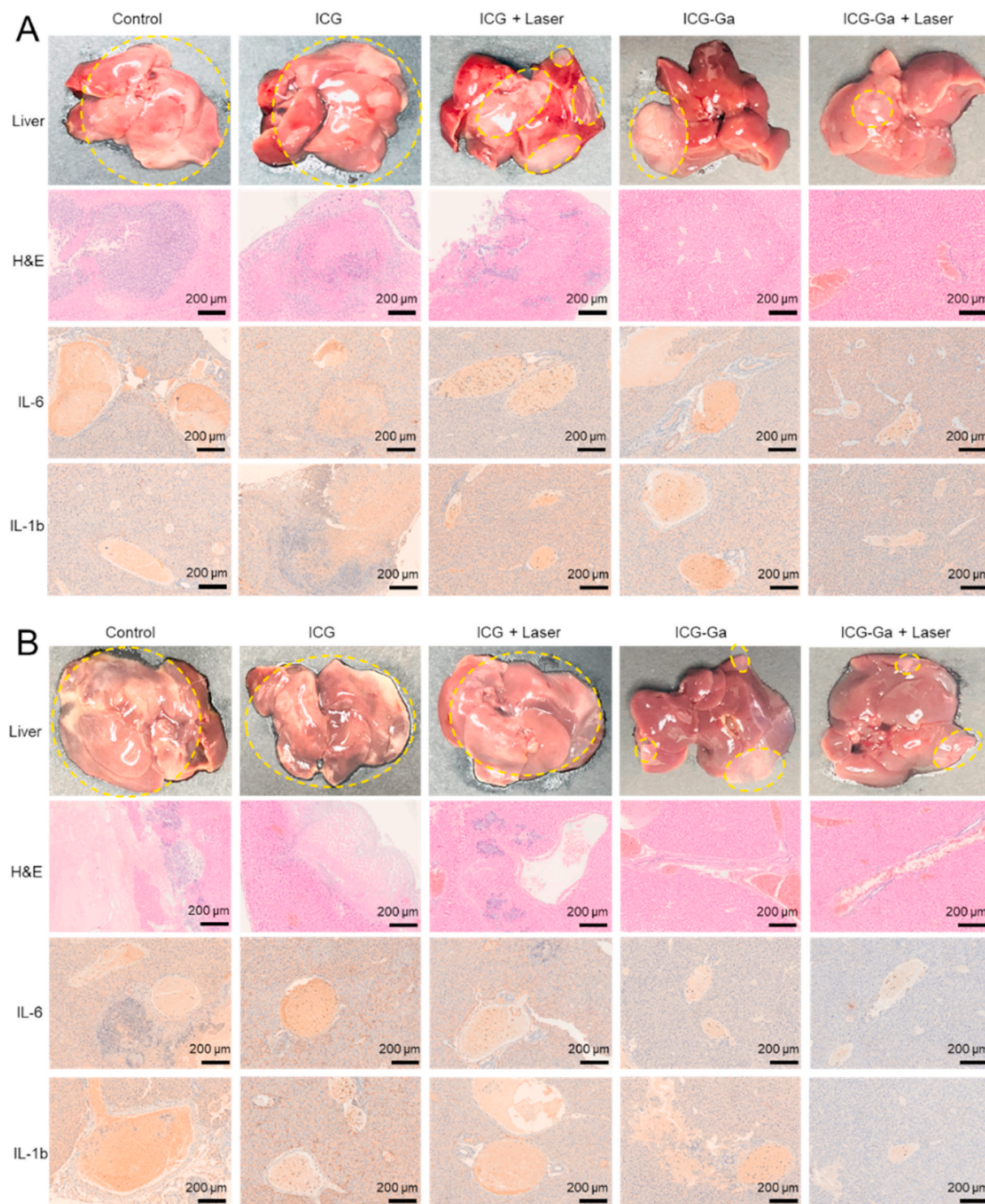

Fig. 5. *In vivo* therapeutic effects of ICG-Ga NPs. Representative photograph, H&E, IL-6, and IL-1b staining of livers section (A) at day 1 and (B) day 3 after various treatments.

number of bacteria. As revealed in Fig. 4D–F, the infected mice had the highest number of bacteria in the livers at the time point of day 1 and day 3 after injection with saline or sole ICG compared with other treatments, and the number of bacteria on day 3 increased significantly in comparison to that of day 1 in all groups. Additionally, the bacterial counts in ICG + Laser and ICG-Ga NPs groups decreased mildly on day 1 and day 3, indicating an enhanced killing efficiency against ESBL *E. coli in vivo*. The ICG-Ga + Laser treatment group exhibited the minimum bacteria counts, displaying the most obvious antibacterial efficiency. Similar experimental results were observed by gram staining (Fig. 4G). That was well consistent with the results *in vitro*, therefore, clearly demonstrating ICG-Ga + Laser treatment possesses the best effective ability to combat ESBL *E. coli*, which was reflected by the minimal number of bacterial clones.

3.5. Anti-inflammation analysis

We then evaluated the pathological changes and related inflammatory indicators of the infectious liver after various treatments. The mice were sacrificed, and livers were collected on day 1 and day 3 for hemotoxilin and eosin (H&E) staining and the inflammatory immunohistochemical staining. Representative photographs of the infectious livers exhibit significant differences between the various treatments (Fig. 5). The livers of mice in the control, ICG, and ICG + Laser groups had more obvious abscess areas on day 1 after ESBL *E. coli* infection (highlight by the yellow dotted line). H&E staining of these livers also exhibited extensive necrosis and inflammatory cell infiltration. Especially for the day 3 after infection, the liver tissue necrosis became more severe with some degree of dissolution and liquefaction in the control, ICG, and ICG + Laser groups. In addition, the expression levels of inflammation factors (IL-6 and IL-1b) in these groups were significantly higher than that in the other groups, including the ICG-Ga NPs group and ICG-Ga + Laser group. The presence of obvious inflammatory foci and necrotic areas indicates the typical inflammatory response. Conspicuously, the degree of inflammation was inhibited and the histopathological conditions were eased dramatically by receiving
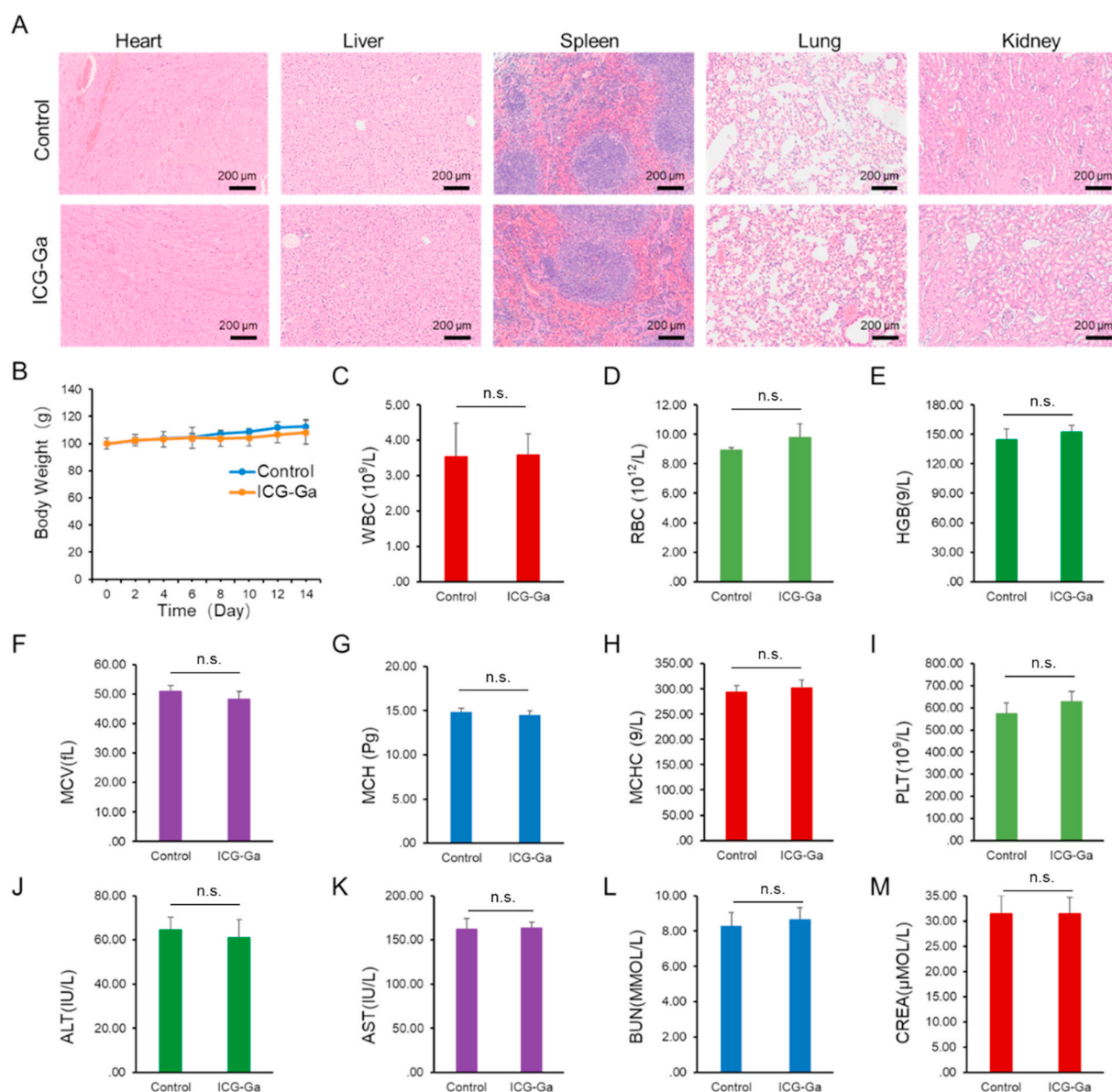
Fig. 6. *In vivo* preliminary toxicity analysis of ICG-Ga NPs. (A) H&E staining of the major organs of mice heart, liver, spleen, lung, and kidney.(B) The changes in body weight of mice after injection with ICG-Ga NPs. (C–M) blood biochemistry and hematology examination, including white blood cells (WBC), red blood cells (RBC), hemoglobin (HGB), mean cell volume (MCV), mean corpuscular hemoglobin (MCH), mean corpuscular hemoglobin concentration (MCHC), blood platelet (PLT), alanine transferase (ALT), aspartate transferase (AST), blood urea nitrogen (BUN), creatinine (CREA). (n.s.: No significant difference, p value > 0.05).

808 nm laser irradiation followed by the injection with ICG-Ga NPs, containing the shrink of abscess area, local suppuration, slight necrosis, the decrease of inflammatory cell infiltration and expression level of IL-6 and IL-1b. Notably, the liver abscess site was basically returned to normal condition after ICG-Ga + Laser treatment, indicating the most effectively histopathological improvement in ESBL *E. coli* infected mice via the combination gallium with ICG-mediated photodynamic therapy.

3.6. Preliminary toxicity analysis

Since Ga-ICG NPs showed excellent *in vitro* biocompatible ability, we further carried out preliminary toxicity analysis. To evaluate the preliminary toxicity of ICG-Ga NPs, the histological analysis of the major organs (Fig. 6A) was conducted on the 14 day after intravenous injection with ICG-Ga NPs at the treatment dose, demonstrating normal tissue structures without appreciable inflammatory lesions or organ damage. It was also found that the body weight of mice in all groups remained similar, indicating no clear acute toxicity of ICG-Ga NPs (Fig. 6B). Similarly, there is no distinct difference in blood biochemistry and hematology parameters, indicating normal liver and kidney functions (Fig. 6C-M). The above result confirmed the ICG-Ga NPs equipping with reliable biosafety *in vivo* could act as an excellent antibacterial agent to inhibit bacteria growth with negligible toxicity at the tested dose. However, more systematic investigations, such as immune-compatibility and long-term toxicity studies, are still needed for future clinical translation.

4. Conclusion

In conclusion, we have developed an efficient strategy to eradicate biofilms and treat bacterial liver abscess by using our non-antibiotic ICG-Ga NPs plus laser irradiation. The excellent antibacterial efficacy was ascribed to the capability of ICG-Ga NPs in converting NIR light to stimulate the toxic ROS generation and destroying iron metabolism, and eventually leading to bacterial cell death. Such a systematic therapeutic nanoagent was effective in inhibiting drug-resistant pathogens both *in vitro* and *in vivo* and could target the liver for curing the infected abscess with negligible systemic toxicities. Thus, the designed strategy offers a potential to generate antibacterial agents for *in vivo* infections.

Declaration of competing interest

The authors declare no competing financial interest.

CRediT authorship contribution statement

Tingting Xie: Conceptualization, Methodology, Data curation, Formal analysis, Writing – original draft. **Yuchen Qi:** Formal analysis, Writing – review & editing. **Yangyang Li:** Methodology, Formal analysis, Writing – review & editing. **Feilu Zhang:** Methodology, Formal analysis, Writing – review & editing. **Wanlin Li:** Formal analysis, Writing – review & editing. **Danni Zhong:** Formal analysis, Writing – review & editing. **Zhe Tang:** Writing – review & editing. **Min Zhou:** Conceptualization, Writing – review & editing, Supervision, Funding acquisition.

Acknowledgements

Appendix A. Supplementary data

Supplementary data to this article can be found online at https://doi.org/10.1016/j.bioactmat.2021.03.032.

References

[1] C.E. Chen, Y.C. Shih, Monomicrobial Klebsiella pneumoniae necrotizing fasciitis with liver abscess: a case report and literature review, Ann. Plast. Surg. 78 (2017) S28–31.

[2] C.T. Fang, S.Y. Lai, W.C. Yi, P.R. Hsueh, K.L. Liu, S.C. Chang, Klebsiella pneumoniae genotype K1: an emerging pathogen that causes septic ocular or central nervous system complications from pyogenic liver abscess, Clin. Infect. Dis. 45 (2007) 284–293.

[3] J.Y. Lee, K.H. Kim, Endogenous endophthalmitis complicated by pyogenic liver abscess: a review of 17 years' experience at a single center, Digestion 90 (2014) 116–121.

[4] L. Meddings, R.P. Myers, J. Hubbard, A.A. Shaheen, K.B. Laupland, E. Dixon, C. Coffin, G.G. Kaplan, A population-based study of pyogenic liver abscesses in the United States: incidence, mortality, and temporal trends, Am. J. Gastroenterol. 105 (2010) 117–124.

[5] E.B. Breidenstein, C. Fuente-Nunez, R.E. Hancock, Pseudomonas aeruginosa: all roads lead to resistance, Trends Microbiol. 19 (2011) 419–426.

[6] H.D. Marston, D.M. Dixon, J.M. Knisely, T.N. Palmore, A.S. Fauci, Antimicrobial resistance, J. Am. Med. Assoc. 316 (2016) 1193–1204.

[7] N. Skovgaard, New trends in emerging pathogens, Int. J. Food Microbiol. 120 (2007) 217–224.

[8] J. Li, R.L. Nation, J.D. Turnidge, R.W. Milne, K. Coulthard, C.R. Rayner, D. L. Paterson, Colistin: the re-emerging antibiotic for multidrug-resistant Gram-negative bacterial infections, Lancet Infect. Dis. 6 (2006) 589–601.

[9] Y. Zhao, Q. Guo, X. Dai, X. Wei, Y. Yu, X. Chen, C. Li, Z. Cao, X. Zhang, A biomimetic non-antibiotic approach to eradicate drug-resistant infections, Adv. Mater. 31 (2019) e1806024.

[10] H.G. Choudhury, Z. Tong, I. Mathavan, Y. Li, S. Iwata, S. Zirah, S. Rebuffat, H. W. Veen, K. Beis, Structure of an antibacterial peptide ATP-binding cassette transporter in a novel outward occluded state, Proc. Natl. Acad. Sci. U. S. A 111 (2014) 9145–9150.

[11] S. Fernandez-Lopez, H.S. Kim, E.C. Choi, M. Delgado, J.R. Granja, A. Khasanov, K. Kraehenbuehl, G. Long, D.A. Weinberger, K.M. Wilcoxen, M.R. Ghadiri, Antibacterial agents based on the cyclic D,L-alpha-peptide architecture, Nature 412 (2001) 452–455.

[12] Z.P. Cheng, X.L. Zhu, Z.L. Shi, K.G. Neoh, E.T. Kang, Polymer microspheres with permanent antibacterial surface from surface-initiated atom transfer radical polymerization, Ind. Eng. Chem. Res. 44 (2005) 7098–7104.

[13] Y. Zhao, Y. Tian, Y. Cui, W. Liu, W. Ma, X. Jiang, Small molecule-capped gold nanoparticles as potent antibacterial agents that target Gram-negative bacteria, J. Am. Chem. Soc. 132 (2010) 12349–12356.

[14] A.M. Allahverdiyev, E.S. Abamor, M. Bagirova, M. Rafailovich, Antimicrobial effects of TiO$_2$ and Ag$_2$O nanoparticles against drug-resistant bacteria and leishmania parasites, Future Microbiol. 6 (2011) 933–940.

[15] F. Natalio, R. Andre, A.F. Hartog, B. Stoll, K.P. Jochum, R. Wever, W. Tremel, Vanadium pentoxide nanoparticles mimic vanadium haloperoxidases and thwart biofilm formation, Nat. Nanotechnol. 7 (2012) 530–535.

[16] D. Das, B.C. Nath, P. Phukon, S.K. Dolui, Synthesis and evaluation of antioxidant and antibacterial behavior of CuO nanoparticles, Colloids Surf. B Biointerfaces 101 (2013) 430–433.

[17] N. Talebian, S.M. Amininezhad, M. Doudi, Controllable synthesis of ZnO nanoparticles and their morphology-dependent antibacterial and optical properties, J. Photochem. Photobiol., B 120 (2013) 66–73.

[18] G. Franci, A. Falanga, S. Galdiero, L. Palomba, M. Rai, G. Morelli, M. Galdiero, Silver nanoparticles as potential antibacterial agents, Molecules 20 (2015) 8856–8874.

[19] J.S. Kim, E. Kuk, K.N. Yu, J.H. Kim, S.J. Park, H.J. Lee, S.H. Kim, Y.K. Park, Y. H. Park, C.Y. Hwang, Y.K. Kim, Y.S. Lee, D.H. Jeong, M.H. Cho, Antimicrobial effects of silver nanoparticles, Nanomed. Nanotechnol. *Biol. Med.* 3 (2007) 95–101.

[20] J.Y. Maillard, P. Hartemann, Silver as an antimicrobial: facts and gaps in knowledge, Crit. Rev. Microbiol. 39 (2013) 373–383.

[21] J.P. Ruparelia, A.K. Chatterjee, S.P. Duttagupta, S. Mukherji, Strain specificity in antimicrobial activity of silver and copper nanoparticles, Acta Biomater. 4 (2008) 707–716.

[22] X. Li, S.M. Robinson, A. Gupta, K. Saha, Z. Jiang, D.F. Moyano, A. Sahar, M. A. Riley, V.M. Rotello, Functional gold nanoparticles as potent antimicrobial agents against multi-drug-resistant bacteria, ACS Nano 8 (2014) 10682–10686.

[23] S.C. Wei, L. Chang, C.C. Huang, H.T. Chang, Dual-functional gold nanoparticles with antimicrobial and proangiogenic activities improve the healing of multidrug-resistant bacteria-infected wounds in diabetic mice, Biomater. Sci. 7 (2019) 4482–4490.

[24] Y. Qiao, F. Ma, C. Liu, B. Zhou, Q. Wei, W. Li, D. Zhong, Y. Li, M. Zhou, Near-infrared laser-excited nanoparticles to eradicate multidrug-resistant bacteria and promote wound healing, ACS Appl. Mater. Interfaces 10 (2018) 193–206.

[25] D. Hu, H. Li, B. Wang, Z. Ye, W. Lei, F. Jia, Q. Jin, K.F. Ren, J. Ji, Surface-adaptive gold nanoparticles with effective adherence and enhanced photothermal ablation of methicillin-resistant Staphylococcus aureus biofilm, ACS Nano 11 (2017) 9330–9339.

[26] Y. Zhao, X. Dai, X. Wei, Y. Yu, X. Chen, X. Zhang, C. Li, Near-infrared light-activated thermosensitive liposomes as efficient agents for photothermal and antibiotic synergistic therapy of bacterial biofilm, ACS Appl. Mater. Interfaces 10 (2018) 14426–14437.

[27] M.I. Setyawati, X. Yuan, J. Xie, D.T. Leong, The influence of lysosomal stability of silver nanomaterials on their toxicity to human cells, Biomaterials 35 (25) (2014) 6707–6715.

[28] K. Zheng, M.I. Setyawati, D.T. Leong, J. Xie, Antimicrobial silver nanomaterials, Coord. Chem. Rev. 357 (2018) 1–17.

[29] K. Zheng, M.I. Setyawati, D.T. Leong, J. Xie, Antimicrobial gold nanoclusters, ACS Nano 11 (2017) 6904–6910.

[30] C.R. Chitambar, Medical applications and toxicities of gallium compounds, Int. J. Environ. Res. Publ. Health 7 (2010) 2337–2361.

[31] C. Bonchi, F. Imperi, F. Minandri, P. Visca, E. Frangipani, Repurposing of gallium-based drugs for antibacterial therapy, Biofactors 40 (2014) 303–312.

[32] C.H. Goss, Y. Kaneko, L. Khuu, G.D. Anderson, S. Ravishankar, M.L. Aitken, N. Lechtzin, G. Zhou, D.M. Czyz, K. McLean, O. Olakanmi, H.A. Shuman, M. Teresi, E. Wilhelm, E. Caldwell, S.J. Salipante, D.B. Hornick, R.J. Siehnel, L. Becker, B. E. Britigan, P.K. Singh, Gallium disrupts bacterial iron metabolism and has therapeutic effects in mice and humans with lung infections, Sci. Transl. Med. 10 (2018), e7520.

[33] Y. Kaneko, M. Thoendel, O. Olakanmi, B.E. Britigan, P.K. Singh, The transition metal gallium disrupts Pseudomonas aeruginosa iron metabolism and has antimicrobial and antibiofilm activity, J. Clin. Invest. 117 (2007) 877–888.

[34] C.R. Chitambar, J. Narasimhan, Targeting iron-dependent DNA synthesis with gallium and transferrin-gallium, Pathobiology: J. Immunopathol., Mol. Cell. Bio. 59 (1991) 3–10.

[35] G. Apseloff, Therapeutic uses of gallium nitrate: past, present, and future, Am. J. Therapeut. 6 (1999) 327–339.

[36] O. Olakanmi, B.E. Britigan, L.S. Schlesinger, Gallium disrupts iron metabolism of mycobacteria residing within human macrophages, Infect. Immun. 68 (10) (2000) 5619–5627.

[37] T. Urade, H. Sawa, Y. Iwatani, T. Abe, R. Fujinaka, K. Murata, Y. Mii, I.M. Man, S. Oka, D. Kuroda, Laparoscopic anatomical liver resection using indocyanine green fluorescence imaging, Asian J. Surg. 9584 (2019) 30220–30229.

[38] M.P. Luciano, J.M. Namgoong, R.R. Nani, S.H. Nam, C. Lee, I.H. Shin, M. J. Schnermann, J. Cha, A biliary tract-specific near-infrared fluorescent dye for image-guided hepatobiliary surgery, Mol. Pharm. 16 (2019) 3253–3260.

[39] H. Wu, C. Wang, J. Sun, L. Sun, J. Wan, S. Wang, D. Gu, C. Yu, C. Yang, J. He, Z. Zhang, Y. Lv, H. Wang, M. Yao, W. Qin, C. Wang, H. Jin, Self-assembled and self-monitored sorafenib/indocyanine green nanodrug with synergistic antitumor activity mediated by hyperthermia and reactive oxygen species-induced apoptosis, ACS Appl. Mater. Interfaces 11 (2019) 43996–44006.

[40] H. Vögeling, S.R. Pinnapireddy, B. Seitz, U. Bakowsky, Indocyanine green loaded PLGA film coated coronary stents for photo-triggered in situ biofilm eradication, Colloid Interface Sci. Commun. 27 (2018) 35–39.

[41] G. Carja, E.F. Grosu, M. Mureseanu, D. Lutic, A family of solar light responsive photocatalysts obtained using Zn^{2+} Me^{3+} (Me = Al/Ga) LDHs doped with Ga_2O_3 and In_2O_3 and their derived mixed oxides: a case study of phenol/4-nitrophenol decomposition, Catal. Sci. Technol. 7 (2017) 5402–5412.

[42] D.S. Lee, S.H. Eom, Y.M. Kim, H.S. Kim, M.J. Yim, S.H. Lee, D.H. Kim, J.Y. Je, Antibacterial and synergic effects of gallic acid-grafted-chitosan with beta-lactams against methicillin-resistant Staphylococcus aureus (MRSA), Can. J. Microbiol. 60 (2014) 629–638.